


Article

Efficient Electrocatalytic Ammonia Synthesis via Theoretical Screening of Titanate Nanosheet-Supported Single-Atom Catalysts

Kaiheng Zhao ¹, Jingnan Wang ¹, Yongan Yang ^{1,*} and Xi Wang ^{2,3,*} 

¹ Institute of Molecular Plus, School of Chemical Engineering and Technology, Tianjin University, Tianjin 300072, China; kh_zhao@163.com (K.Z.); wjn10081711@163.com (J.W.)

² Key Laboratory of Luminescence and Optical Information, Ministry of Education, School of Physical Science and Engineering, Beijing Jiaotong University, Beijing 100044, China

³ Tangshan Research Institute of Beijing Jiaotong University, Tangshan 063000, China

* Correspondence: revned_yang@tju.edu.cn (Y.Y.); xiwang@bjtu.edu.cn (X.W.)

Abstract: The electrocatalytic nitrogen reduction reaction (NRR) for synthesizing ammonia holds promise as an alternative to the traditional high-energy-consuming Haber–Bosch method. Rational and accurate catalyst design is needed to overcome the challenge of activating N₂ and to suppress the competitive hydrogen evolution reaction (HER). Single-atom catalysts have garnered widespread attention due to their 100% atom utilization efficiency and unique catalytic performance. In this context, we constructed theoretical models of metal single-atom catalysts supported on titanate nanosheets (M-TiNS). Initially, density functional theory (DFT) was employed to screen 12 single-atom catalysts for NRR- and HER-related barriers, leading to the identification of the theoretically optimal NRR catalyst, Ru-TiNS. Subsequently, experimental synthesis of the Ru-TiNS single-atom catalyst was successfully achieved, exhibiting excellent performance in catalyzing NRR, with the highest NH₃ yield rate reaching 15.19 μmol mg_{cat}⁻¹ h⁻¹ and a Faradaic efficiency (FE) of 15.3%. The combination of experimental results and theoretical calculations demonstrated the efficient catalytic ability of Ru sites, validating the effectiveness of the constructed theoretical screening process and providing a theoretical foundation for the design of efficient NRR catalysts.

Keywords: NRR; single-atom catalysts; theoretical screening



Citation: Zhao, K.; Wang, J.; Yang, Y.; Wang, X. Efficient Electrocatalytic Ammonia Synthesis via Theoretical Screening of Titanate Nanosheet-Supported Single-Atom Catalysts. *Materials* **2024**, *17*, 2239. <https://doi.org/10.3390/ma17102239>

Academic Editor: Ramón Manuel Fernández Domene

Received: 29 March 2024

Revised: 6 May 2024

Accepted: 7 May 2024

Published: 9 May 2024



Copyright: © 2024 by the authors. Licensee MDPI, Basel, Switzerland. This article is an open access article distributed under the terms and conditions of the Creative Commons Attribution (CC BY) license (<https://creativecommons.org/licenses/by/4.0/>).

1. Introduction

Hydrogen (H₂), serving as a clean energy carrier, exhibits high efficiency and zero emissions, rendering it an ideal energy substance [1,2]. However, the challenge of hydrogen storage severely restricts its applications [3–5]. Concurrently, ammonia (NH₃), functioning as a hydrogen source, boasts a higher hydrogen density (contains 17.8 wt% H), implying that it can store the same quantity of hydrogen in a smaller volume [6–8]. Moreover, NH₃ can liberate hydrogen through facile catalytic decomposition or thermal decomposition [9,10]; hence, NH₃ holds promise in addressing hydrogen storage and distribution issues [11]. Nevertheless, the conventional Haber–Bosch process suffers from high energy consumption and pollution [12,13], necessitating the urgent development of greener and more convenient synthetic methodologies. In contrast, electrocatalytic nitrogen reduction for NH₃ synthesis reaction (NRR) features mild reaction conditions, directly utilizing H₂O as a proton source, and harnessing the benefits of renewable energy sources such as wind and solar power [14], thereby offering potential to supplant traditional NH₃ synthesis techniques. However, the formidable N≡N bond (941 kJ mol⁻¹) and the competitive hydrogen evolution reaction (HER) significantly curtail the industrial application of NRR [15,16]. Consequently, the development of novel catalysts capable of efficiently adsorbing and activating N₂ while concurrently suppressing HER holds immense application value.

TiO₂ is widely used as a catalyst support in various reactions due to its economy, structural stability, and environmental friendliness [17,18]. These reactions include the oxygen evolution reaction (OER) [19], HER [20,21], nitrate reduction reaction (NO₃RR) [22], and urea synthesis through CO₂ + N₂ coupling [23]. Generally, pure TiO₂ lacks active sites for effective activation of reactants. Therefore, people often introduce active species (Cu [24], Pt [25], Fe [26], Au [27], etc.) into TiO₂ carriers through doping to enhance the catalyst's activity. There are also relevant reports in NRR; for example, Zhao et al. introduced phosphorus atoms into TiO₂ nanorods to increase the catalyst's activity by forming more oxygen vacancies. In 0.1 M LiClO₄ electrolyte, a NH₃ yield rate of 23.05 μmol mg_{cat}⁻¹ h⁻¹ and a Faradaic efficiency of 12.26% were achieved at -0.3 V vs. RHE potential [28]. Yang et al. introduced Au nanoparticles into TiO₂ nanosheets to accelerate charge transfer in the reaction, altering the local electronic structure to effectively adsorb and activate N₂. Ultimately, at -0.4 V vs. RHE potential, a NH₃ yield rate of 12.5 μmol mg_{cat}⁻¹ h⁻¹ and a Faradaic efficiency of 10.2% were achieved [27]. Although these catalysts have shown decent catalytic performance, further improvement is still needed. Moreover, what is more important is that these studies are only aimed at specific elements; in other words, the selection of catalyst active sites lacks a more rational and accurate effective design.

Therefore, in our work, we first used titanate nanosheets (TiNS) as a carrier to design 12 single-atom catalyst M-TiNS (M = Fe, Co, Ni, Cu, Ru, Rh, Pd, Ag, Os, Ir, Pt, Au). Initially, we calculated the adsorption energy of N₂ on single-atom catalyst M-TiNS, confirming that all could adsorb N₂, with Ru-TiNS and Os-TiNS exhibiting the most negative adsorption energies. Subsequently, based on the first hydrogenation of N₂ in NRR and HER as selection criteria, the energy barriers corresponding to each M-TiNS were calculated, confirming that Ru-TiNS and Rh-TiNS had the optimal energy barriers for the first hydrogenation of N₂ and HER (the lower N₂ first hydrogenation barrier and the higher HER barrier). Taking these two catalysts as examples, we calculated the Gibbs free energy of the entire reaction pathway. Among the two reaction pathways, Ru-TiNS exhibited the lowest reaction barrier, suggesting that Ru-TiNS would demonstrate superior NRR performance. Subsequently, we successfully synthesized the Ru-TiNS single-atom catalyst experimentally and demonstrated its excellent NRR performance through electrochemical experiments (NH₃ yield rate: 15.19 μmol mg_{cat}⁻¹ h⁻¹, Faradaic efficiency: 15.3%), which was approximately 10 times higher than that of pure TiNS. Through experiments, electronic density of states analysis, COHP calculations, and other methods, we confirmed good electron transfer between Ru sites and N₂, thereby effectively activating N₂ and catalyzing subsequent hydrogenation steps. Through these steps, we developed a method combining theoretical prediction with experiments to obtain excellent NRR catalysts, providing new and effective ideas for the design of novel NRR catalysts.

2. Materials and Methods

2.1. Density Functional Theory Calculation

All DFT calculations were conducted using the Vienna ab initio simulation package (VASP version 5.4.4) code [29,30]. The Perdew–Burke–Ernzerhof (PBE) functional within generalized gradient approximation (GGA) was employed to handle the exchange–correlation interactions [31]. The projector augmented wave (PAW) method was chosen to describe ion–electron interaction [32]. The plane-wave basis cutoff energy was set to 500 eV. The convergence thresholds of energy and force were set to 1 × 10⁻⁵ eV and 0.02 eV Å⁻¹, respectively. A vacuum thickness of 20 Å was applied to avoid periodic interplanar interactions. The charge density difference was visualized by using the VESTA code. The Bader algorithm was employed to calculate the charge transfer and charge distribution. Additionally, for orbital-resolved chemical bonding analysis, we utilized the crystal orbital Hamilton population (COHP) method through the LOBSTER package. This method projects the PAW wave functions onto atomic-like basis functions [33–36].

The Gibbs free energy was calculated using the following equation:

$$G = E + E_{ZPE} - T\Delta S \quad (1)$$

The electronic energy is denoted by E , and the zero-point energy is represented as E_{ZPE} ($E_{ZPE} = 1/2\sum\hbar\nu$, where ν is the normal mode vibrational frequency and \hbar is the reduced Planck constant). The entropy correction is designated as $T\Delta S$ (with T set at 298 K). All $T\Delta S$ values involved are obtained through VASPKIT using DFT-calculated frequencies, while those for gaseous molecules are sourced from the NIST-JANAF thermodynamic tables.

2.2. Chemicals and Material

All reagents used in the synthesis and experimental processes were not further purified. Potassium carbonate (K_2CO_3), potassium bicarbonate ($KHCO_3$), lithium carbonate (Li_2CO_3), and titanium dioxide (TiO_2 , Rutile) were purchased from Alfa Aesar. Ruthenium oxide (RuO_2) was from Acros. Tetrabutylammonium hydroxide (TBAOH) and the ammonium ion standard solution (1000 $\mu\text{g}/\text{mL}$) were purchased from Shanghai Aladdin Biochemical Technology Co., Ltd. (Shanghai, China).

2.3. Synthesis of TiNS and Ru-TiNS Nanosheets

TiO_2 , Li_2CO_3 , and K_2CO_3 were ground in a mortar at the mole ratio in the formula ($K_{0.8}Ti_{1.73}Li_{0.27}O_4$) for 30 min. The ground powder was calcined at 800 °C for 20 h in air. And then, the sample was ground for another 30 min and calcined at 800 °C for 20 h in air again to obtain layered titanate. The second step was protonation to form layered TiO_2 with extended interlayer distance. A total of 1 g titanate powder was dispersed in 100 mL HCl (1.5 M). The HCl needed to be replaced three times every 48 h. Then, $H_{0.7}Ti_{1.825}O_4$ was exfoliated through dispersion in a 0.03 M tetrabutylammonium hydroxide (TBAOH) solution on a table concentrator for a duration of 10 days. The ratio of the TBAOH solution to $H_{0.7}Ti_{1.825}O_4$ was maintained at 300 mL g^{-1} . Finally, the precipitate was obtained by centrifugation, followed by thorough washing with ultrapure water to achieve a neutral pH and remove excess TBAOH. After freeze-drying for three days, fluffy titanate ultra-thin nanosheets (TiNS) were obtained.

The distinguishing factor of Ru-TiNS was the combination of several raw materials (RuO_2 , TiO_2 , Li_2CO_3 , and K_2CO_3) in accordance with a specific molar ratio, with a molar fraction of 0.1 for the metal component.

2.4. Characterizations

The structure and morphology of several catalysts were characterized by X-ray diffraction (XRD, Bruker D2 diffractometer with Cu $K\alpha$ radiation, Billerica, MA, USA), Scanning Electron Microscopy (SEM, Hitachi S-4800 field emission SEM, Tokyo, Japan), Transmission Electron Microscopic (TEM, Thermofisher Talos F200X with acceleration voltage of 200 kV, Waltham, MA, USA), and High Angle Annular Dark Field Scanning Transmission Electron Microscopy (HAADF-STEM, FEI Tecnai G2 F20, Waltham, MA, USA). The X-ray Photoelectron Spectroscopy (XPS) analysis was performed on a Thermo ESCALAB 250Xi electron spectrometer with 300 W Al KR radiation (Waltham, MA, USA).

2.5. Electrocatalytic Nitrogen Reduction Reaction (NRR) Experiment

All electrochemical characterizations were carried out using the CHI 760E (Chenhua, Shanghai, China) electrochemical workstation. A three-electrode system was employed with a platinum foil serving as the counter electrode, a saturated Ag/AgCl reference electrode, and the working electrode. A H-type electrochemical cell was utilized, separated by a Nafion 117 proton exchange membrane. Prior to use, the Nafion proton exchange membrane was boiled in a 5% H_2O_2 aqueous solution at 80 °C for 1 h and subjected to multiple rinses. The carbon paper used was treated before usage with a mixed solution of H_2SO_4 and H_2O_2 (1:3, vol.) for 12 h, followed by several rinses to remove surface impurities. It was then trimmed to a size of $1 \times 3 \text{ cm}^2$ for later use. The catalyst ink was

prepared by adding 5 mg of the catalyst and 30 μL of a 5% Nafion solution to a mixture of 500 μL ethanol and 470 μL water, followed by 1 h of sonication. The working electrode was created by evenly applying 60 μL of the catalyst ink (0.3 mg of catalyst) to carbon paper ($0.3 \times 1 \text{ cm}^2$), and allowed to air-dry naturally. The electrolyte solution was 0.1 M KHCO_3 . The potential was converted to RHE using the following equation: $E \text{ (vs. RHE)} = E \text{ (vs. Ag/AgCl)} + 0.0591 \times \text{pH} + 0.197$. Before the test, N_2 (30 mL min^{-1}) was injected for 30 min, and other gas interference was discharged. Cyclic voltammetry (CV) was performed at a potential range of 0.3–0.5 V vs. RHE at a scan rate of 50 mV s^{-1} to stabilize the electrode. Subsequently, linear sweep voltammetry (LSV) was carried out at a scan rate of 10 mV s^{-1} , followed by chronoamperometry (CA) testing.

The generated NH_3 was quantitatively analyzed using the indophenol blue method [37]. A total of 2 mL post-reaction electrolyte was taken from the cathode chamber. Then, 1 mL of the diluted electrolyte was mixed with 2 mL of 1.0 M NaOH solution (including 5 wt% salicylic acid and 5 wt% sodium citrate), followed by the addition of 1 mL of 0.05 M NaClO solution and 0.2 mL of 1 wt% sodium nitroprusside solution. After thorough mixing, the mixture was allowed to stand at room temperature for 2 h. UV-Vis absorption spectroscopy data were collected at a wavelength of 655 nm. Subsequently, the concentration of NH_3 was calculated using a standard curve.

The NH_3 yield rate ($\mu\text{g h}^{-1} \text{ mg}_{\text{cat}}^{-1}$) is calculated using the following formula:

$$\text{Yield rate}_{\text{NH}_3} = (C_{\text{NH}_3} \times V) / (t \times m_{\text{cat}})$$

The Faradaic Efficiency (FE) for NH_3 is calculated using the following formula:

$$\text{FE}_{\text{NH}_3} = \frac{3 \times C_{\text{NH}_3} \times V \times F \times 10^{-6}}{17 \times Q} \times 100\%$$

In this equation, C_{NH_3} represents the concentration of NH_3 detected in the catholyte ($\mu\text{g mL}^{-1}$); V is the volume of the catholyte in the cathode compartment (30 mL); t stands for the reaction time (1 h); m_{cat} indicates the mass of the loaded catalyst (mg); F is Faraday's constant ($96,485 \text{ C mol}^{-1}$); and Q refers to the total charge transferred during the reaction (C).

3. Results and Discussion

3.1. Theoretical Screening

All models of M-TiNS catalysts were created by substituting M atoms for five-coordinate Ti atoms in the lattice, which has been confirmed in previous studies [38]. The lattice parameters are $a = 14.99 \text{ \AA}$ and $b = 12.11 \text{ \AA}$, with a vacuum layer of 20 \AA added in the c direction to prevent periodic interlayer interactions (Figure 1a,b). Group VIII and IB transition metals were selected as the active centers to construct single-atom catalysts, and the corresponding structures are shown in Figure S1.

The prerequisite for the nitrogen reduction reaction (NRR) is the efficient adsorption and activation of N_2 at the active site. Figure 1c shows the adsorption energy of N_2 on M-TiNS, with the corresponding adsorption structures depicted in Figure S2. The results indicate that all catalysts adopt an end-on adsorption model for N_2 , and their adsorption energies are negative values, suggesting that the process is exothermic and stable. Notably, the Ru and Os-TiNS catalysts exhibit adsorption energies of -1.21 eV and -1.28 eV , respectively. The adsorption energies for other catalysts are around -0.3 eV . This suggests that N_2 adsorption is most stable on these two catalysts. Concurrently, we computed the post-adsorption N-N bond length; for all catalysts, the N-N bond is elongated following N_2 adsorption, exceeding the ideal N_2 molecule's 1.10 \AA (Figure S3), which signifies effective activation of the N_2 molecule. Subsequently, the average bond lengths for M-N and Ti-N were tallied (Figure S4), oscillating between 2.1 and 2.8 \AA , which is less than the distance characteristic of van der Waals interactions, confirming the likelihood of the N_2 adsorption being chemisorptive in nature. Bader charge analysis

revealed directional electron transfer from the M atoms to the N_2 molecule (Figure S5). Furthermore, the trend in the quantity of charge transfer differed from that of the bond length (or adsorption energy), which could be attributed to the influence of spin electrons.

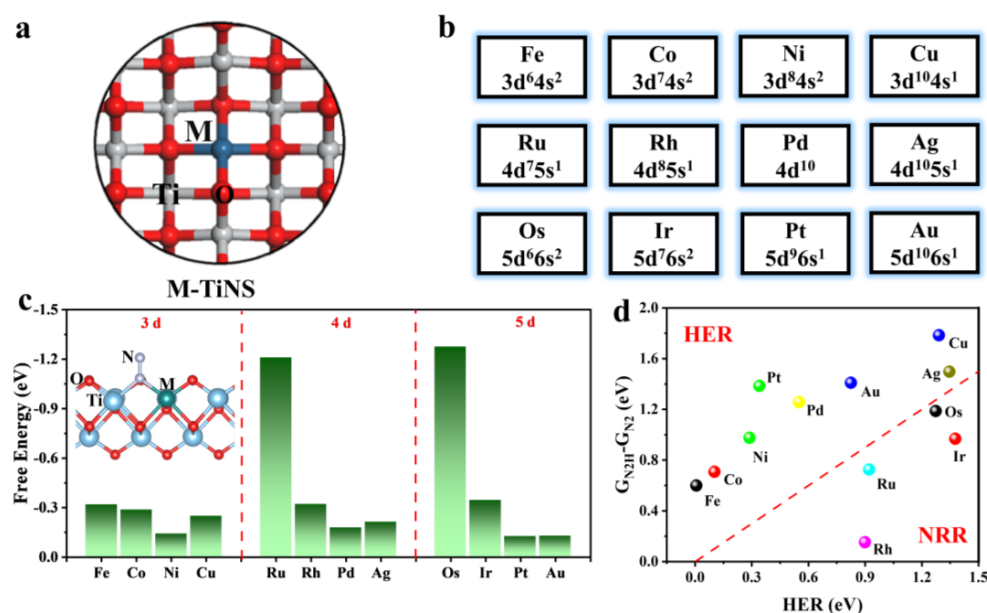


Figure 1. (a) Presents the top view of the M-TiNS model, employed for introducing the M element into TiNS, as shown in (b). (c) Free energy of N_2 adsorption on M-TiNS. The illustration depicts the adsorption configuration of N_2 . (d) The selectivity of NRR over HER is delineated by the changes in Gibbs free energy (ΔG) for the initial hydrogenation of N_2 ($N_2 + H^+ + e^- \rightarrow NNH$) and hydrogen recombination ($H^+ + e^- \rightarrow 1/2H_2$) on M-TiNS, displayed along the horizontal and vertical axes, respectively. The dashed line in the figure represents the equality of ΔG for the two processes.

During the N_2 electrocatalysis process, the HER (hydrogen evolution reaction) is unavoidable; it competes with the NRR for protons and electrons in the electrolyte, leading to a decrease in NRR activity. The free energy of $*H$ is significantly affected by the applied electric field, primarily due to its involvement in proton and electron transfer. In contrast, the adsorption process of N_2 lacks proton and electron transfer, and its free energy is unaffected by the electric potential. Therefore, we compared the free energies of N_2 hydrogenation to NNH and H recombination to evaluate the selectivity of the catalysts (Figures S6 and S7). As shown in Figure 1d, most catalysts exhibit a catalytic activity in HER that significantly affects the Faradaic efficiency of NRR, promoting hydrogen production via HER. However, Rh, Ru, Os, and Ir-TiNS catalysts mainly promote NRR. Nonetheless, Os and Ir-TiNS catalysts with hydrogenation barriers greater than 0.8 eV were excluded. Consequently, Rh and Ru-TiNS catalysts emerge as promising candidates for effectively suppressing HER in ammonia synthesis.

As is widely recognized, there are two probable reaction mechanisms for NRR: the distal hydrogenation mechanism (PATH-I) [39] and the alternating hydrogenation mechanism (PATH-II) [40] (Figure 2a). In the distal pathway, the proton–electron pair initially attacks the distal nitrogen atom consecutively to release one molecule of NH_3 , followed by an attack on the second nitrogen atom to release a second NH_3 molecule, thus completing the reaction. Conversely, in the alternating pathway, the proton–electron pair alternately attacks the two nitrogen atoms to simultaneously form two NH_3 molecules.

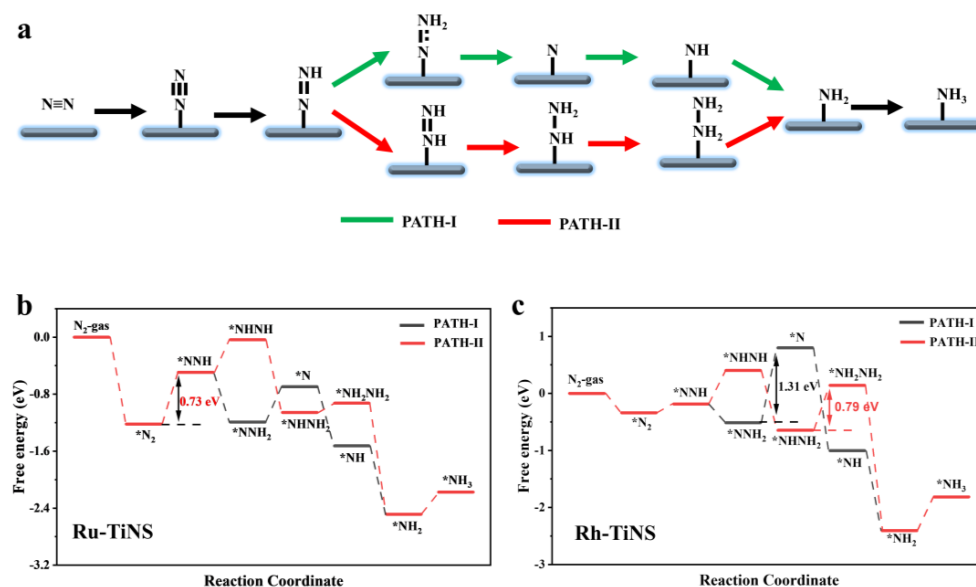


Figure 2. (a) Illustrated schematically are the distal and alternating pathways for NRR. (b,c) Gibbs free energy profiles for the electroreduction of N_2 on Ru-TiNS and Rh-TiNS.

Figure 2b,c show the Gibbs free energy diagrams for the NRR on Ru and Rh-TiNS catalysts via the distal and alternating pathways. The configurations of the relevant reaction intermediates are presented in Figures S8 and S9. Initially, the adsorption of N_2 on the catalysts is an end-on process and exothermic. Subsequently, the $*N_2$ is attacked by a proton–electron pair (H^+/e^-) to form $*NNH$, completing the first hydrogenation step. The Gibbs free energy changes (ΔG) for Ru and Rh-TiNS are 0.73 eV and 0.15 eV, respectively. For the Ru-TiNS catalyst, this represents the rate-determining step (RDS) for both PATH-I and PATH-II. Thereafter, $*NNH$ undergoes further attack by H^+/e^- , with two possible outcomes: formation of either the $*NHNH$ or $*NNH_2$ intermediate. The formation of $*NHNH$ on Ru and Rh-TiNS requires the absorption of 0.46 eV and 0.59 eV of energy, respectively, while the formation of $*NNH_2$ is exothermic. Thus, both catalysts complete the reaction via PATH-I. Following this, $*NNH_2$ is attacked by H^+/e^- to form the $*N$ intermediate and release one molecule of NH_3 . This step is endothermic for both catalysts, with ΔG values of 0.50 and 1.31 eV, respectively. For the Rh-TiNS catalyst, this is the RDS for the entire reaction process (path-I). Furthermore, in the case of Rh-TiNS in path-II, the RDS barrier is 0.79 eV ($NHNH_2 \rightarrow NH_2NH_2$). Given that the RDS for Rh-TiNS is substantially higher than that for Ru-TiNS, only the Ru-TiNS catalyst is discussed henceforth. After the release of the first NH_3 molecule, $*N$ undergoes a three-step protonation process, i.e., $*N \rightarrow *NH \rightarrow *NH_2 \rightarrow *NH_3$, to produce the second NH_3 molecule. The first two steps are exothermic, while the third step requires the absorption of 0.31 eV. Subsequently, the Bader charges of the intermediates during the reaction process were calculated (Figure S10).

3.2. Characterization of Model Catalyst (Ru-TiNS)

Due to the implications from theoretical calculations suggesting the potentially excellent NRR performance of Ru-TiNS, we embarked on the experimental synthesis of Ru-TiNS, aiming to validate the conclusions drawn from theoretical computations.

Following our previous methodology [38,41], Ru-doped TiNS catalyst was synthesized using a combination of solid-state grinding, calcination, ion exchange, and soft-template stripping techniques. Inductively coupled plasma optical emission spectrometry (ICP-OES) characterization confirmed the Ru loading to be 3.6 wt%. Initially, X-ray diffraction (XRD) patterns (Figure 3a) revealed characteristic off-plane diffraction peaks of typical 0k0 ($k = 1, 2, 3$) stacked layered structures in Ru-TiNS [23,42–44]. Further visual examination via scanning electron microscopy (SEM) (Figure 3b) displayed the distinct layered structure

of Ru-TiNS. This result is consistent with the SEM images of pure TiNS (Figure S11), and combined with their similar BET surface areas (Figure S12), it suggests that the introduction of Ru does not lead to morphological differences. Moreover, a high-resolution transmission electron microscopy (HRTEM) image illustrated its ultrathin layered structure (Figure 3c). Through high-angle annular dark-field scanning TEM (HAADF-STEM) imaging, no aggregated Ru species were detected, consistent with the corresponding elemental mapping results. (Figure 3d). To gain deeper insights into the state of Ru, aberration-corrected TEM characterization was performed. As depicted in Figure 3e, Ru atoms were uniformly distributed within the TiNS lattice through replacing Ti atoms, consistent with the theoretical model constructed. X-ray photoelectron spectroscopy (XPS) analysis revealed characteristic peaks attributed to Ru³⁺ species at a binding energy of 281.1 and 285.7 eV, indicating the Ru species were in the +3 valance state (Figure 3f) [45]. This result is consistent with the Ru 3p XPS (Figure S13) [46]. It can be observed that compared to the original RuO₂ with a +4 valance state, Ru was partially reduced. Furthermore, through XPS spectra of Ti and O, it can be observed that, compared to pure TiNS support, characteristic peaks of Ti and O have shifted towards higher binding energies, indicating partial electron transfer from the TiNS support to Ru [47–52], which is consistent with the change in the valence state of Ru. (Figure 4a,b). This phenomenon indicated a strong interaction between Ru and the TiNS support. Furthermore, from the XPS spectrum of O, it can be observed that the introduction of Ru also leads to an increase in oxygen vacancies (O_{vac}), suggesting that Ru replaces Ti in the TiO₆ octahedral sites, forming unsaturated coordination structures of RuO_x (x < 6), consistent with the structure predicted by our theoretical modeling. Drawing from these characterization findings, we ascertain the successful synthesis of single-atom Ru-doped ultrathin layered TiNS catalyst.

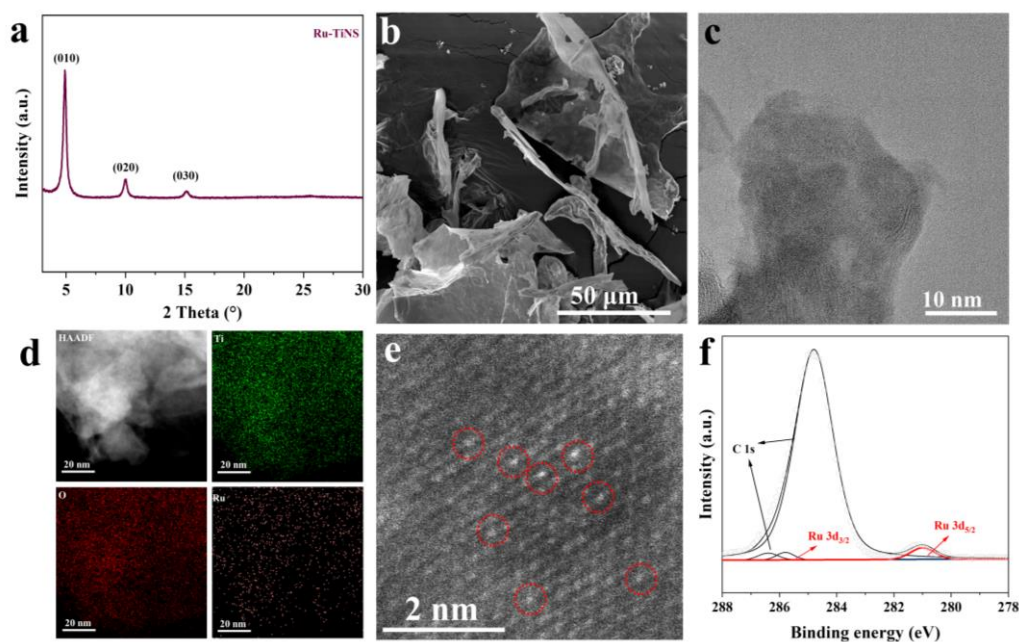


Figure 3. Structural characterization of the synthesized model catalyst Ru-TiNS. XRD pattern of Ru-TiNS (a), SEM image (b), and HRTEM image (c). (d) EDS element mappings of the Ru-TiNS catalyst. (e) Aberration-corrected HAADF-STEM image, where the Ru single atoms are highlighted by red circles. (f) High-resolution XPS spectrum of Ru in Ru-TiNS.

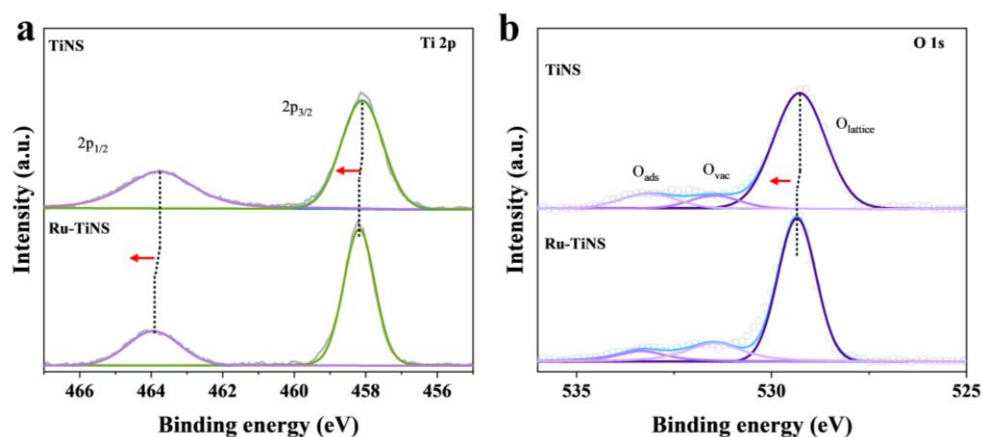


Figure 4. (a) High-resolution XPS spectrum of Ti in Ru-TiNS and TiNS. (b) High-resolution XPS spectrum of O in Ru-TiNS and TiNS.

3.3. NRR Performance Test of Ru-TiNS

To evaluate the performance of Ru-TiNS for electrocatalytic N_2 reduction to produce NH_3 , we employed a H-type electrolysis cell and utilized carbon paper (CP) loaded with Ru-TiNS as the working electrode, forming a three-electrode system alongside a saturated Ag/AgCl reference electrode and a platinum foil electrode serving as the counter electrode. A 0.1 M $KHCO_3$ solution saturated with N_2 was used as the electrolyte, with continuous N_2 flow (30 mL min^{-1}) throughout the testing period. Prior to testing, cyclic voltammetry (CV) tests were conducted in the non-Faradaic region (0.3–0.4 V vs. RHE) until stability was achieved to activate the electrode.

Firstly, linear sweep voltammetry (LSV) tests were performed in the potential range of -1 to 0 V vs. RHE to preliminarily assess the catalytic activity of Ru-TiNS under different atmospheres. As shown in Figure 5a, under an argon atmosphere, the reaction occurring on Ru-TiNS is HER. Compared to the current density curve obtained after Ar saturation of the electrolyte, Ru-TiNS exhibited higher current density under N_2 atmosphere. Moreover, compared to pure CP, Ru-TiNS showed a significant increase in current density, indicating its promising NRR catalytic activity. To quantitatively analyze the catalytic performance of Ru-TiNS, we conducted chronoamperometry (CA) tests at different potentials for 1 h. As shown in Figure S14, with increasingly negative potentials, the current density also increased, suggesting more vigorous reactions occurring on the electrode surface. After 1 h of reaction, quantitative analysis of NH_3 concentration in the electrolyte was performed using the indophenol blue method combined with standard curves (Figures S15 and S16), as shown in Figure 5b,c. It can be observed that the NH_3 yield corresponding to Ru-TiNS exhibited a volcano-shaped relationship with potential. The highest NH_3 yield ($15.19 \mu\text{mol mgcat}^{-1} \text{ h}^{-1}$) and satisfactory Faradaic efficiency (15.3%) were achieved at -0.3 V vs. RHE. The Watt and Chrisp method was used to detect potential byproduct N_2H_4 [53], and the results indicated the absence of N_2H_4 (Figure S17). Additionally, we calculated the FE of H_2 (Figure S18), which increased as the potential became more negative. At higher potentials, N_2 activation was ineffective due to insufficient driving force, while at lower potentials, competition from hydrogen evolution reactions led to a decrease in NRR performance, as inferred from the reduced Faradaic efficiency and NH_3 yield after -0.3 V vs. RHE. To verify the source of the product, various experiments were designed (Figure S19). At -0.3 V vs. RHE, when using pure CP as the working electrode, NH_3 was not detected in the product; however, NH_3 was only detected when N_2 was introduced during the reaction with Ru-TiNS as the working electrode, and no NH_3 was detected after one hour of electrolysis at open circuit potential (OCP). Combined with the absence of external nitrogen in the catalyst, it can be concluded that NH_3 in the product originates from the introduced N_2 . Furthermore, to determine the active center, CA tests were conducted on pure TiNS support, as shown in Figure 5d. It can be observed that at the optimal potential of -0.3 V vs. RHE, TiNS exhibited a NH_3 yield

of only $1.23 \mu\text{mol mgcat}^{-1} \text{h}^{-1}$, with a corresponding FE of 1.5%. In comparison, the NH_3 yield and FE of Ru-TiNS were increased by ~ 10 times, indicating that the introduction of Ru effectively enhances the catalyst's activity. By comparing the catalytic performance with the pure TiNS support, we demonstrate that the ultrathin TiNS support lacks the ability to catalyze NRR. This further supports that the NRR active sites on Ru-TiNS are attributed to Ru sites. Additionally, we further tested the activity of RuO_2 and found that RuO_2 has almost no catalytic activity. By comparing it with Ru-TiNS, we demonstrate that the unique chemical structure of Ru sites in the synthesized Ru-TiNS contributes to its excellent catalytic activity in the NRR process. In the 10 h long-term stability test (Figure 5e), there was no significant decay in the corresponding current density of Ru-TiNS, demonstrating the excellent stability of the Ru-TiNS catalyst.

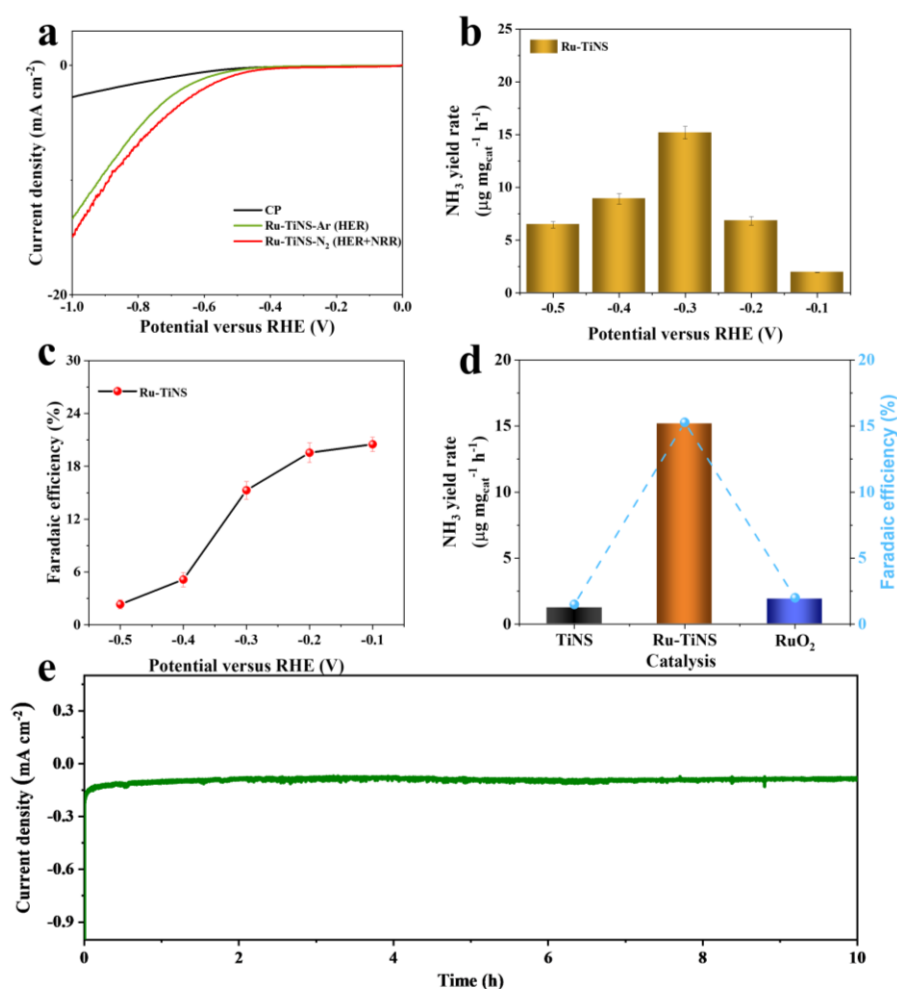


Figure 5. Electrocatalytic NRR performance of TiNS and Ru-TiNS. (a) Linear sweep voltammetry curves of CP in electrolyte saturated with nitrogen, Ru-TiNS in electrolyte saturated with argon, and electrolyte saturated with nitrogen. (b) NH_3 yield of Ru-TiNS at different potentials (b) and Faradaic efficiency (c). (d) Comparison of catalytic performance between TiNS, RuO_2 , and Ru-TiNS at -0.3V vs. RHE. (e) Stability test of Ru-TiNS at -0.3V vs. RHE for 10 h.

Subsequently, to evaluate the electrochemical active area of Ru-TiNS, CV tests were conducted in the non-Faradaic region, obtaining the CV curves of Ru-TiNS catalyst and pure TiNS support at different scan rates (Figure S20). By linear fitting of the difference in current density and scan rate in the CV curves, the slope of the straight line obtained represents the electrochemical double-layer capacitance (C_{dl}) [54]. The C_{dl} values of Ru-TiNS and pure TiNS support were 9.94 mF cm^{-2} and 0.66 mF cm^{-2} , respectively. A larger

C_{dl} value indicates that Ru-TiNS exposes more catalytic active sites, further confirming the role of Ru as the active site.

Furthermore, EIS impedance tests were conducted on Ru-TiNS and TiNS separately, as shown in the Nyquist plot in Figure S21. Both exhibited semicircles in the high-frequency range of the impedance spectrum. The radius of the semicircle in the plot corresponding to Ru-TiNS was much smaller than that of TiNS, indicating more intense electron transfer between Ru and N_2 , consistent with the theoretical calculations mentioned below [55].

3.4. Interaction between Ru-TiNS and Reactants

In order to further understand the interaction between N_2 and Ru-TiNS, the density of states (DOS) was calculated initially. As shown in Figure 6a, Ru-TiNS exhibits significant spin polarization, with the up-spin orbitals substantially higher than the down-spin orbitals, possessing an absolute spin of $2 \mu_B$. Upon the adsorption of N_2 , the spin of Ru-TiNS vanishes, which evidences the substantial impact of spin electrons in the N_2 activation process (Figures S22 and S23). What is more, the unoccupied d orbitals of Ru-TiNS accept electrons from the σ and π orbitals of N_2 , which are in proximity to the Fermi level. This is likely due to the principal involvement of Ru-up orbitals, leading to their reduction and even appearance below the Fermi level, thus forming a bonded state and enhancing N_2 adsorption. Furthermore, the occupied d orbital electrons of Ru-TiNS are returned to the π^* orbitals of N_2 , leading to partial occupancy and expansion below the Fermi level of N_2 . In other words, the activation of N_2 follows an “acceptance-donation” mechanism [56]. Simultaneously, Figure 6d presents a schematic of this process. As depicted in Figure 6b, the charge density difference further verifies this mechanism, with the feedback mechanism playing a dominant role, resulting in a net charge transfer of $0.40e$ from Ru-TiNS to N_2 .

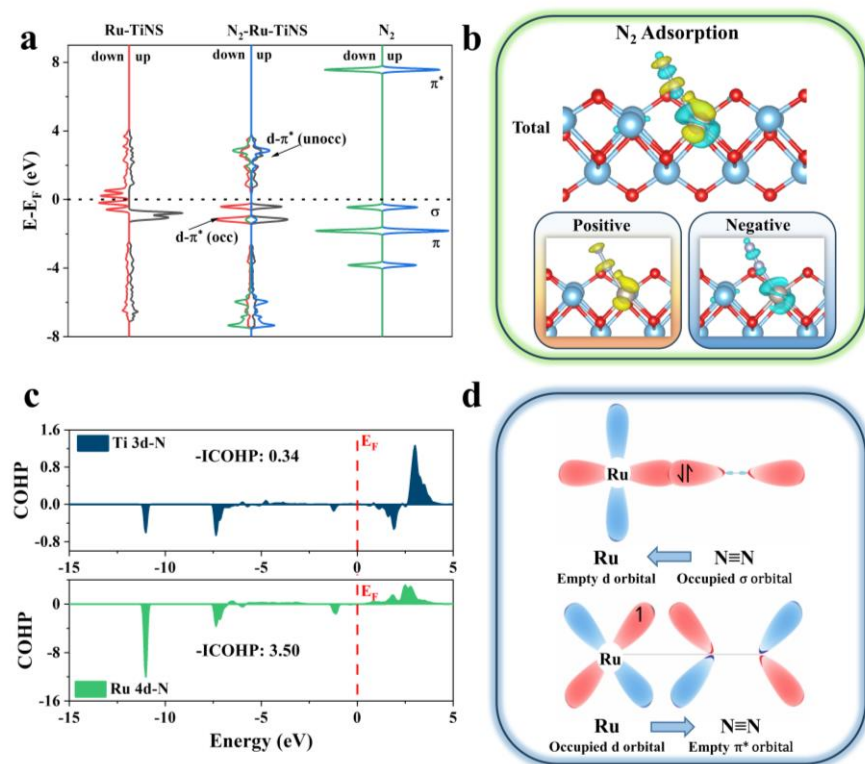


Figure 6. (a) The density of states (DOS) diagrams for free N_2 , Ru-TiNS, and N_2 adsorbed on Ru-TiNS. (b) The charge density distribution after N_2 adsorption on Ru-TiNS. Blue and yellow represent charge depletion and charge accumulation, respectively. (c) The crystal orbital Hamilton populations (COHP) for N_2 adsorbed on Ru-TiNS. (d) A schematic illustration of the interaction between N_2 and Ru-TiNS.

Moreover, COHP reveals the strength of the d- π interaction, with -ICOHP given quantitatively. For the adsorbed configuration of N₂, the -ICOHP values for Ti 3d-N and Ru 4d-N are 0.34 and 3.50, respectively (Figure 6c). The disparity greater than an order of magnitude confirms the decisive role of Ru incorporation in the reactivity of N₂.

4. Conclusions

In summary, to obtain a superior NRR catalyst, we conducted theoretical screening of 12 M-TiNS catalysts and confirmed that Ru-TiNS had the optimal NRR rate-determining step energy barrier, as well as a higher HER energy barrier, implying that Ru-TiNS exhibits excellent NRR catalytic performance and can suppress the occurrence of the HER reaction. Subsequently, at the experimental level, we successfully synthesized the Ru-TiNS single-atom catalyst and found through electrochemical testing that Ru-TiNS exhibited outstanding activity at -0.3 V vs. RHE: NH₃ yield rate, reaching 15.19 $\mu\text{mol mg}_{\text{cat}}^{-1} \text{h}^{-1}$ and a Faradaic efficiency (FE) of 15.3%. This performance is approximately 10 times higher than that of pure TiNS. Through electronic density of states analysis and COHP analysis, we confirmed good electron transfer between Ru and N₂, enabling N₂ activation and hydrogenation. Through these findings, we have successfully developed a method aimed at providing unique insights and approaches for the rational design and synthesis of efficient NRR catalysts.

Supplementary Materials: The following supporting information can be downloaded at: <https://www.mdpi.com/article/10.3390/ma17102239/s1>, Figure S1: The adsorption configurations of M-TiNS; Figure S2: The adsorption configurations of N₂ on M-TiNS; Figure S3: N-N bond length after N₂ adsorption; Figure S4: M-N bond length after N₂ adsorption; Figure S5: Charge changes after N₂ adsorption; Figure S6: The adsorption configurations of *H on M-TiNS; Figure S7: The adsorption configurations of *NNH on M-TiNS; Figure S8: Configuration of intermediates in N₂ reduction reaction on Ru-TiNS; Figure S9: Configuration of intermediates in N₂ reduction reaction on Rh-TiNS; Figure S10: Bader charges of intermediates along the reaction coordinates for in N₂ reduction reaction on Ru-TiNS; Figure S11: SEM image of pure TiNS support; Figure S12: Nitrogen adsorption-desorption isotherms and their corresponding surface area of TiNS (a) and Ru-TiNS (b); Figure S13: High-resolution Ru 3p XPS spectrum of Ru in Ru-TiNS; Figure S14: The i-t curves obtained from chronoamperometry tests at different potentials; Figure S15: The UV-visible absorption curves corresponding to the coloration of indophenol blue after reaction with NH₄⁺ of different concentrations; Figure S16: The linear fitting curves of absorbance at 655 nm after coloration by the indophenol blue method for NH₄⁺ of different concentrations; Figure S17: UV-Vis absorbance curves of Ru-TiNS before and after electrolysis at -0.3 V vs. RHE; Figure S18: FE_{H₂} of Ru-TiNS at different potentials; Figure S19: NH₃ yield rates under different conditions including pure carbon paper (-0.3 V vs. RHE), open circuit potential, only Ar bubbling (-0.3 V vs. RHE), and N₂ bubbling (-0.3 V vs. RHE); Figure S20: CV curves obtained for pure TiNS (a) and Ru-TiNS (b) at different scan rates, along with the corresponding calculated double-layer capacitances (c); Figure S21: Electrochemical impedance spectroscopy (EIS) of Ru-TiNS and TiNS; Figure S22: The Spin charge density of (a) Ru-TiNS and (b) N₂ adsorption on Ru-TiNS; Figure S23: The projected density of (a) Free N₂, (b) Ru 4d in Ru-TiNS, and (c,d) N₂ molecule adsorbed on Ru-TiNS.

Author Contributions: Formal analysis, investigation, data curation, writing—original draft preparation, K.Z.; methodology, conceptualization and software, J.W.; visualization and investigation, Y.Y.; supervision, writing—review and editing, X.W. All authors have read and agreed to the published version of the manuscript.

Funding: This research was funded by Science and Technology Project of Guangdong Province: 2020B0101370001.

Institutional Review Board Statement: Not applicable.

Informed Consent Statement: Not applicable.

Data Availability Statement: Data are contained within the article.

Conflicts of Interest: The authors declare that they have no known competing financial interests or personal relationships that could have appeared to influence the work reported in this paper.

References

1. Dutta, I.; Parsapur, R.K.; Chatterjee, S.; Hengne, A.M.; Tan, D.; Peramaiah, K.; Solling, T.I.; Nielsen, O.J.; Huang, K.-W. The role of fugitive hydrogen emissions in selecting hydrogen carriers. *ACS Energy Lett.* **2023**, *8*, 3251–3257. [[CrossRef](#)]
2. Pivovar, B.; Rustagi, N.; Satyapal, S. Hydrogen at scale (H₂@Scale): Key to a clean, economic, and sustainable energy system. *Electrochem. Soc. Interface* **2018**, *27*, 47–52. [[CrossRef](#)]
3. Allendorf, M.D.; Stavila, V.; Snider, J.L.; Witman, M.; Bowden, M.E.; Brooks, K.; Tran, B.L.; Autrey, T. Challenges to developing materials for the transport and storage of hydrogen. *Nat. Chem.* **2022**, *14*, 1214–1223. [[CrossRef](#)] [[PubMed](#)]
4. Wang, Z.; Wang, Y.; Afshan, S.; Hjalmarsson, J. A review of metallic tanks for H₂ storage with a view to application in future green shipping. *Int. J. Hydrogen Energy* **2021**, *46*, 6151–6179. [[CrossRef](#)]
5. Lu, R.; Rao, D.; Lu, Z.; Qian, J.; Li, F.; Wu, H.; Wang, Y.; Xiao, C.; Deng, K.; Kan, E.; et al. Prominently improved hydrogen purification and dispersive metal binding for hydrogen storage by substitutional doping in porous graphene. *J. Phys. Chem. C* **2012**, *116*, 21291–21296. [[CrossRef](#)]
6. Sørensen, R.Z.; Hummelshøj, J.S.; Klerke, A.; Reves, J.B.; Vegge, T.; Nørskov, J.K.; Christensen, C.H. Indirect, Reversible high-density hydrogen storage in compact metal ammine salts. *J. Am. Chem. Soc.* **2008**, *130*, 8660–8668. [[CrossRef](#)] [[PubMed](#)]
7. Awad, O.I.; Zhou, B.; Harrath, K.; Kadrigama, K. Characteristics of NH₃/H₂ blend as carbon-free fuels: A review. *Int. J. Hydrogen Energy* **2023**, *48*, 38077–38100. [[CrossRef](#)]
8. Guo, J.; Chen, P. Catalyst: NH₃ as an energy carrier. *Chem* **2017**, *3*, 709–712. [[CrossRef](#)]
9. Wang, L.; Yi, Y.; Zhao, Y.; Zhang, R.; Zhang, J.; Guo, H. NH₃ decomposition for H₂ generation: Effects of cheap metals and supports on plasma-catalyst synergy. *ACS Catal.* **2015**, *5*, 4167–4174. [[CrossRef](#)]
10. Dirtu, D.; Odochian, L.; Pui, A.; Humelnicu, I. Thermal decomposition of ammonia. N₂H₄-an intermediate reaction product. *Open Chem.* **2006**, *4*, 666–673. [[CrossRef](#)]
11. Chang, F.; Gao, W.; Guo, J.; Chen, P. Emerging materials and methods toward ammonia-based energy storage and conversion. *Adv. Mater.* **2021**, *33*, 2005721. [[CrossRef](#)] [[PubMed](#)]
12. Hollevoet, L.; Jardali, F.; Gorbanev, Y.; Creel, J.; Bogaerts, A.; Martens, J.A. Towards green ammonia synthesis through plasma-driven nitrogen oxidation and catalytic reduction. *Angew. Chem. Int. Ed.* **2020**, *59*, 23825–23829. [[CrossRef](#)] [[PubMed](#)]
13. Wang, M.; Khan, M.A.; Mohsin, I.; Wicks, J.; Ip, A.H.; Sumon, K.Z.; Dinh, C.-T.; Sargent, E.H.; Gates, I.D.; Kibria, M.G. Can sustainable ammonia synthesis pathways compete with fossil-fuel based Haber–Bosch processes? *Energy Environ. Sci.* **2021**, *14*, 2535–2548. [[CrossRef](#)]
14. Hasan, A.; Dincer, I. Development of an integrated wind and PV system for ammonia and power production for a sustainable community. *J. Clean. Prod.* **2019**, *231*, 1515–1525. [[CrossRef](#)]
15. Zhao, Y.; Li, F.; Li, W.; Li, Y.; Liu, C.; Zhao, Z.; Shan, Y.; Ji, Y.; Sun, L. Identification of M-NH₂-NH₂ intermediate and rate determining step for nitrogen reduction with bioinspired sulfur-bonded few catalyst. *Angew. Chem. Int. Ed.* **2021**, *60*, 20331–20341. [[CrossRef](#)]
16. Zhao, X.; Hu, G.; Chen, G.F.; Zhang, H.; Zhang, S.; Wang, H. Comprehensive understanding of the thriving ambient electrochemical nitrogen reduction reaction. *Adv. Mater.* **2021**, *33*, 2007650. [[CrossRef](#)]
17. Xing, Z.; Zhang, J.; Cui, J.; Yin, J.; Zhao, T.; Kuang, J.; Xiu, Z.; Wan, N.; Zhou, W. Recent advances in floating TiO₂-based photocatalysts for environmental application. *Appl. Catal. B Environ.* **2018**, *225*, 452–467. [[CrossRef](#)]
18. Ge, M.; Cai, J.; Iocozzia, J.; Cao, C.; Huang, J.; Zhang, X.; Shen, J.; Wang, S.; Zhang, S.; Zhang, K.-Q.; et al. A review of TiO₂ nanostructured catalysts for sustainable H₂ generation. *Int. J. Hydrogen Energy* **2017**, *42*, 8418–8449. [[CrossRef](#)]
19. Deng, Z.; Li, L.; Ren, Y.; Ma, C.; Liang, J.; Dong, K.; Liu, Q.; Luo, Y.; Li, T.; Tang, B.; et al. Highly efficient two-electron electroreduction of oxygen into hydrogen peroxide over Cu-doped TiO₂. *Nano Res.* **2022**, *15*, 3880–3885. [[CrossRef](#)]
20. Nong, S.; Dong, W.; Yin, J.; Dong, B.; Lu, Y.; Yuan, X.; Wang, X.; Bu, K.; Chen, M.; Jiang, S.; et al. Well-dispersed ruthenium in mesoporous crystal TiO₂ as an advanced electrocatalyst for hydrogen evolution reaction. *J. Am. Chem. Soc.* **2018**, *140*, 5719–5727. [[CrossRef](#)] [[PubMed](#)]
21. Nie, M.; Sun, H.; Liao, J.; Li, Q.; Xue, Z.; Xue, F.; Liu, F.; Wu, M.; Gao, T.; Teng, L. Study on the catalytic performance of Pd/TiO₂ electrocatalyst for hydrogen evolution reaction. *Int. J. Hydrogen Energy* **2021**, *46*, 6441–6447. [[CrossRef](#)]
22. Yang, L.; Wang, C.; Li, Y.; Ge, W.; Tang, L.; Shen, J.; Zhu, Y.; Li, C. Frustrated Lewis Pairs on Zr single atoms supported N-doped TiO_{2-x} catalysts for electrochemical nitrate reduction to ammonia. *Adv. Funct. Mater.* **2024**, 2401094. [[CrossRef](#)]
23. Pan, L.; Wang, J.; Lu, F.; Liu, Q.; Gao, Y.; Wang, Y.; Jiang, J.; Sun, C.; Wang, J.; Wang, X. Single-atom or dual-atom in TiO₂ nanosheet: Which is the better choice for electrocatalytic urea synthesis? *Angew. Chem. Int. Ed.* **2023**, *62*, e202216835. [[CrossRef](#)]
24. Yang, X.; Wang, R.; Wang, S.; Song, C.; Lu, S.; Fang, L.; Yin, F.; Liu, H. Sequential active-site switches in integrated Cu/Fe-TiO₂ for efficient electroreduction from nitrate into ammonia. *Appl. Catal. B Environ.* **2023**, *325*, 122360. [[CrossRef](#)]
25. Lv, J.; Tian, Z.; Dai, K.; Ye, Y.; Liang, C. Interface and defect engineer of titanium dioxide supported palladium or platinum for tuning the activity and selectivity of electrocatalytic nitrogen reduction reaction. *J. Colloid Interf. Sci.* **2019**, *553*, 126–135. [[CrossRef](#)]
26. Song, G.; Gao, R.; Zhao, Z.; Zhang, Y.; Tan, H.; Li, H.; Wang, D.; Sun, Z.; Feng, M. High-spin state Fe(III) doped TiO₂ for electrocatalytic nitrogen fixation induced by surface F modification. *Appl. Catal. B Environ.* **2022**, *301*, 120809. [[CrossRef](#)]

27. Yang, P.; Guo, H.; Wu, H.; Zhang, F.; Liu, J.; Li, M.; Yang, Y.; Cao, Y.; Yang, G.; Zhou, Y. Boosting charge-transfer in tuned Au nanoparticles on defect-rich TiO₂ nanosheets for enhancing nitrogen electroreduction to ammonia production. *J. Colloid Interf. Sci.* **2023**, *636*, 184–193. [[CrossRef](#)] [[PubMed](#)]
28. Zhao, P.; Zhang, L.; Song, J.; Wen, S.; Cheng, Z. Phosphorus cation substitution in TiO₂ nanorods toward enhanced N₂ electroreduction. *Appl. Surf. Sci.* **2020**, *523*, 146517. [[CrossRef](#)]
29. Kresse, G.; Furthmüller, J. Efficiency of ab-initio total energy calculations for metals and semiconductors using a plane-wave basis set. *Comput. Mater. Sci.* **1996**, *6*, 15–50. [[CrossRef](#)]
30. Kresse, G.; Furthmüller, J. Efficient iterative schemes for ab initio total-energy calculations using a plane-wave basis set. *Phys. Rev. B* **1996**, *54*, 11169–11186. [[CrossRef](#)]
31. Perdew, J.P.; Burke, K.; Ernzerhof, M. Generalized gradient approximation made simple. *Phys. Rev. Lett.* **1996**, *77*, 3865–3868. [[CrossRef](#)]
32. Blöchl, P.E. Projector augmented-wave method. *Phys. Rev. B* **1994**, *50*, 17953–17979. [[CrossRef](#)]
33. Nelson, R.; Ertural, C.; George, J.; Deringer, V.L.; Hautier, G.; Dronskowski, R. LOBSTER: Local orbital projections, atomic charges, and chemical-bonding analysis from projector-augmented-wave-based density-functional theory. *J. Comput. Chem.* **2020**, *41*, 1931–1940. [[CrossRef](#)]
34. Maintz, S.; Deringer, V.L.; Tchougréeff, A.L.; Dronskowski, R. LOBSTER: A tool to extract chemical bonding from plane-wave based DFT. *J. Comput. Chem.* **2016**, *37*, 1030–1035. [[CrossRef](#)] [[PubMed](#)]
35. Deringer, V.L.; Tchougréeff, A.L.; Dronskowski, R. Crystal orbital hamilton population (COHP) analysis as projected from plane-wave basis sets. *J. Phys. Chem. A* **2011**, *115*, 5461–5466. [[CrossRef](#)] [[PubMed](#)]
36. Dronskowski, R.; Blochl, P.E. Crystal orbital Hamilton populations (COHP): Energy-resolved visualization of chemical bonding in solids based on density-functional calculations. *J. Phys. Chem.* **2002**, *97*, 8617–8624. [[CrossRef](#)]
37. Li, L.; Tang, C.; Yao, D.; Zheng, Y.; Qiao, S.-Z. Electrochemical nitrogen reduction: Identification and elimination of contamination in electrolyte. *ACS Energy Lett.* **2019**, *4*, 2111–2116. [[CrossRef](#)]
38. Lu, F.; Wang, J.; Gao, Y.; Wang, Y.; Wang, X. Engineering Pt-Cu diatomics electrocatalysts enables highly efficient urea synthesis. *AIChE J.* **2024**, e18403. [[CrossRef](#)]
39. Tayyebi, E.; Abghoui, Y.; Skúlason, E. Elucidating the mechanism of electrochemical N₂ reduction at the Ru(0001) electrode. *ACS Catal.* **2019**, *9*, 11137–11145. [[CrossRef](#)]
40. Feng, X.; Liu, J.; Chen, L.; Kong, Y.; Zhang, Z.; Zhang, Z.; Wang, D.; Liu, W.; Li, S.; Tong, L.; et al. Hydrogen radical-induced electrocatalytic N₂ reduction at a low potential. *J. Am. Chem. Soc.* **2023**, *145*, 10259–10267. [[CrossRef](#)] [[PubMed](#)]
41. Yi, D.; Lu, F.; Zhang, F.; Liu, S.; Zhou, B.; Gao, D.; Wang, X.; Yao, J. Regulating charge transfer of lattice oxygen in single-atom-doped titania for hydrogen evolution. *Angew. Chem. Int. Ed.* **2020**, *59*, 15855–15859. [[CrossRef](#)] [[PubMed](#)]
42. Wang, J.; Yang, R.; Liu, Q.; Yang, Y.; Wang, X. Enhancing electrocatalytic ammonia synthesis through theoretical design of cluster catalysts supported on TiO₂ surface. *Mater. Today Energy* **2024**, *39*, 101466. [[CrossRef](#)]
43. Sasaki, T.; Watanabe, M. Osmotic swelling to exfoliation. Exceptionally high degrees of hydration of a layered titanate. *J. Am. Chem. Soc.* **1998**, *120*, 4682–4689. [[CrossRef](#)]
44. Sasaki, T.; Watanabe, M.; Hashizume, H.; Yamada, H.; Nakazawa, H. Macromolecule-like aspects for a colloidal suspension of an exfoliated titanate. Pairwise association of nanosheets and dynamic reassembling process initiated from it. *J. Am. Chem. Soc.* **1996**, *118*, 8329–8335. [[CrossRef](#)]
45. Morgan, D.J. Resolving ruthenium: XPS studies of common ruthenium materials. *Surf. Interface Anal.* **2015**, *47*, 1072–1079. [[CrossRef](#)]
46. Citrin, P.H.; Ginsberg, A.P. X-ray photoemission from the Creutz-Taube mixed valence complex: A reassessment. *J. Am. Chem. Soc.* **2002**, *103*, 3673–3679. [[CrossRef](#)]
47. Tian, M.; Jiang, Z.; Chen, C.; Kosari, M.; Li, X.; Jian, Y.; Huang, Y.; Zhang, J.; Li, L.; Shi, J.-W.; et al. Engineering Ru/MnCo₃O_x for 1,2-dichloroethane benign destruction by strengthening C–Cl cleavage and chlorine desorption: Decisive role of H₂O and Reaction Mechanism. *ACS Catal.* **2022**, *12*, 8776–8792. [[CrossRef](#)]
48. Li, J.; Yi, D.; Zhan, F.; Zhou, B.; Gao, D.; Guo, D.; Liu, S.; Wang, X.; Yao, J. Monolayered Ru₁/TiO₂ nanosheet enables efficient visible-light-driven hydrogen evolution. *Appl. Catal. B Environ.* **2020**, *271*, 118925. [[CrossRef](#)]
49. Sakamoto, K.; Hayashi, F.; Sato, K.; Hirano, M.; Ohtsu, N. XPS spectral analysis for a multiple oxide comprising NiO, TiO₂, and NiTiO₃. *Appl. Surf. Sci.* **2020**, *526*, 146729. [[CrossRef](#)]
50. Chuang, S.H.; Gao, R.H.; Wang, D.Y.; Liu, H.P.; Chen, L.M.; Chiang, M.Y. Synthesis and characterization of ilmenite-type cobalt titanate powder. *J. Chin. Chem. Soc.* **2013**, *57*, 932–937. [[CrossRef](#)]
51. Wang, Y.-w.; Yuan, P.-H.; Fan, C.-M.; Wang, Y.; Ding, G.-Y.; Wang, Y.-F. Preparation of zinc titanate nanoparticles and their photocatalytic behaviors in the photodegradation of humic acid in water. *Ceram. Int.* **2012**, *38*, 4173–4180. [[CrossRef](#)]
52. Chuang, S.H.; Gao, R.H.; Gao, K.H.; Chiang, M.Y.; Chao, T.S. Formation and structural characterization of cobalt titanate thin films. *J. Chin. Chem. Soc.* **2013**, *57*, 1022–1026. [[CrossRef](#)]
53. Xu, W.; Fan, G.; Chen, J.; Li, J.; Zhang, L.; Zhu, S.; Su, X.; Cheng, F.; Chen, J. Nanoporous palladium hydride for electrocatalytic N₂ reduction under ambient conditions. *Angew. Chem. Int. Ed. Engl.* **2020**, *59*, 3511–3516. [[CrossRef](#)] [[PubMed](#)]
54. Fang, B.; Wang, X.; Zhang, S.; Zhang, L.; Zhang, R.; Wang, K.; Song, S.; Zhang, H. Boosting electrochemical nitrogen fixation via regulating surface electronic structure by CeO₂ hybridization. *Small* **2024**, 2310268. [[CrossRef](#)]

55. Mushtaq, M.A.; Kumar, A.; Yasin, G.; Tabish, M.; Arif, M.; Ajmal, S.; Raza, W.; Naseem, S.; Zhao, J.; Li, P.; et al. Multivalent sulfur vacancy-rich NiCo₂S₄@MnO₂ urchin-like heterostructures for ambient electrochemical N₂ reduction to NH₃. *Small* **2024**, *3*, e2310431. [[CrossRef](#)]
56. Ling, C.; Niu, X.; Li, Q.; Du, A.; Wang, J. Metal-free single atom catalyst for N₂ fixation driven by visible light. *J. Am. Chem. Soc.* **2018**, *140*, 14161–14168. [[CrossRef](#)] [[PubMed](#)]

Disclaimer/Publisher's Note: The statements, opinions and data contained in all publications are solely those of the individual author(s) and contributor(s) and not of MDPI and/or the editor(s). MDPI and/or the editor(s) disclaim responsibility for any injury to people or property resulting from any ideas, methods, instructions or products referred to in the content.